ACS Chemical Neuroscience

Research Article

pubs.acs.org/chemneuro

A New Method To Image Heme-Fe, Total Fe, and Aggregated Protein Levels after Intracerebral Hemorrhage

Mark J. Hackett,[†] Mauren DeSouza,[‡,§] Sally Caine,[∥] Brian Bewer,[⊥] Helen Nichol,[∥] Phyllis G. Paterson,[#] and Frederick Colbourne*[,‡]

[†]Molecular and Environmental Sciences Group, Department of Geological Sciences, University of Saskatchewan, 114 Science Place, Saskatoon, Saskatchewan S7N 5E2, Canada

[‡]Department of Psychology and Neuroscience and Mental Health Institute, University of Alberta, Edmonton, Alberta T6G 2E9, Canada

[§]Stress, Memory and Behaviour Lab, Graduate Program in Biochemistry, Federal University of Pampa, Uruguaiana, Rio Grande do Sul 97500-970, Brazil

[∥]Department of Anatomy and Cell Biology, University of Saskatchewan, 107 Wiggins Road, Saskatoon, Saskatchewan S7N 5E5, Canada

[⊥]Canadian Light Source, Saskatoon, Saskatchewan S7N 2V3, Canada

[#]College of Pharmacy and Nutrition, University of Saskatchewan, D Wing Health Sciences, 107 Wiggins Road, Saskatoon, Saskatchewan S7N 5E5, Canada

Supporting Information

ABSTRACT: An intracerebral hemorrhage (ICH) is a devastating stroke that results in high mortality and significant disability in survivors. Unfortunately, the underlying mechanisms of this injury are not yet fully understood. After the primary (mechanical) trauma, secondary degenerative events contribute to ongoing cell death in the peri-hematoma region. Oxidative stress is thought to be a key reason for this delayed injury, which is likely due to free-Fe-catalyzed free radical reactions. Unfortunately, this is difficult to prove with conventional biochemical assays that fail to differentiate between alterations that occur within the hematoma and peri-hematoma zone. This is a critical limitation, as the hematoma contains tissue severely damaged by the initial hemorrhage and is unsalvageable, whereas the peri-hematoma region is less damaged but at risk from secondary degenerative events. Such events include oxidative stress mediated by free Fe presumed to originate from hemoglobin breakdown. Therefore, minimizing the damage caused by oxidative stress following hemoglobin breakdown and Fe release is a major therapeutic target. However, the extent to which free Fe contributes to the pathogenesis of ICH remains unknown. This investigation used a novel imaging approach that employed resonance Raman spectroscopic mapping of hemoglobin, X-ray fluorescence microscopic mapping of total Fe, and Fourier transform infrared spectroscopic imaging of aggregated protein following ICH in rats. This multimodal spectroscopic approach was used to accurately define the hematoma/peri-hematoma boundary and quantify the Fe concentration and the relative aggregated protein content, as a marker of oxidative stress, within each region. The results revealed total Fe is substantially increased in the hematoma (0.90 μg cm^{-2}), and a subtle but significant increase in Fe that is not in the chemical form of hemoglobin is present within the peri-hematoma zone (0.32 μg cm^{-2}) within 1 day of ICH, relative to sham animals (0.22 μg cm^{-2}). Levels of aggregated protein were significantly increased within both the hematoma (integrated band area 0.10 AU) and peri-hematoma zone (integrated band area 0.10 AU) relative to sham animals (integrated band area 0.056 AU), but no significant difference in aggregated protein content was observed between the hematoma and peri-hematoma zone. This result suggests that the chemical form of Fe and its ability to generate free radicals is likely to be a more critical predictor of tissue damage than the total Fe content of the tissue. Furthermore, this article describes a novel approach to colocalize nonheme Fe and aggregated protein in the peri-hematoma zone following ICH, a significant methodological advancement for the field.

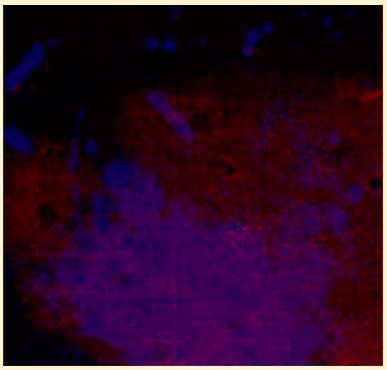

KEYWORDS: *Spectroscopic imaging, intracerebral hemorrhage, stroke, iron, oxidative stress, hemoglobin*

An intracerebral hemorrhage (ICH) is a devastating stroke. ICH mortality is higher than that for ischemic stroke, and survivors are often permanently disabled. ICH can result from a range of conditions such as hypertension, amyloid angiopathy, drug abuse, as a secondary event to coagulation disorders,

Received: August 28, 2014
Published: February 19, 2015

DOI: 10.1021/acschemneuro.5b00037
ACS Chem. Neurosci. 2015, 6, 761−770

ischemic transformation, arteriovenous malformation, traumatic brain injury, tumors, or aneurysms.[1] ICH creates several pathophysiological conditions within the brain, such as inflammation, increased water content (brain swelling or edema) and raised intracranial pressure, neurotoxicity, and potentially ischemic conditions that surround the hematoma.[2−4] All of these events may damage brain tissue and contribute to neuron death following hemorrhagic stroke.

Although the initial hemorrhage into the brain parenchyma is a major cause of tissue damage (primary damage), prolonged (secondary) neuronal death is known to occur following hemorrhagic stroke in both humans and animal models.[2,5−7] This observation has stimulated interest in identifying mechanisms of secondary damage, notably the hypothesis that reactive free Fe accumulates in the parenchyma following erythrocyte lysis and hemoglobin breakdown, thereby propagating damage.[8−10] The brain has several endogenous mechanisms to minimize tissue damage, which use proteins and mobile cells (microglia and macrophages) to sequester or transport free Fe released by hemoglobin degradation.[8,9,11] Macrophages keep much of this iron within phagosomes prior to its ultimate storage in ferritin. However, saturation of the intracellular Fe storage mechanisms would result in elevated free Fe content, which catalyzes free radical production and mediates oxidative stress through classic Fenton chemistry pathways. Although Fe-mediated oxidative stress has not conclusively been proved to be responsible for ongoing neuron death following ICH, it is widely accepted that a zone of at risk tissue surrounds the hematoma (i.e., peri-hematoma zone), and there are clear signs of sublethal and lethal injury occurring here over time.[12] Thus, a major aim of stroke research has been to minimize or prevent neuron death in the peri-hematoma zone through development of therapies that will minimize the toxicity of chemical species (i.e., free Fe) that spread from the hematoma.

Although Fe-mediated toxicity seems to be a likely cause of tissue damage, much remains unknown about the exact biochemical mechanisms and their time course that contribute to neuron death within the peri-hematoma zone following ICH. Indeed, the extent that Fe contributes to tissue damage within the peri-hematoma zone after ICH remains a point of controversy. For example, some studies find that iron chelators reduce injury,[13−15] whereas others do not.[16−19] Besides this controversy, a significant limitation of previous work has been the inability to image, quantify, and correlate the distribution of hemoglobin, total Fe, and markers of oxidative stress (i.e., oxidized protein) in the same sample. By definition, the peri-hematoma zone begins at the boundary of the hematoma, which is the furthest extent that blood penetrates into the brain parenchyma. Histology, specifically to identify the presence of erythrocytes in the brain parenchyma, is conventionally used to define the hematoma boundary. However, as the spread of blood is irregular, definitive assessment of the hematoma/peri-hematoma boundary is difficult in both fresh and fixed sections. Discrimination between the hematoma and peri-hematoma zone is impossible when using traditional biochemical assays of dissected tissue. For example, biochemical assay of total Fe, heme-Fe, and nonheme-Fe requires homogenization of dissected tissue, which cannot be performed with sufficient anatomical precision to precisely delineate the hematoma/peri-hematoma boundary. Dissection often results in contamination of the peri-hematoma zone with hematoma tissue, which produces artificially high measurements of Fe concentration. Alternatively, a conservative peri-hematoma boundary may be used to ensure that no hematoma tissue is sampled. However, this approach fails to detect important biochemical changes in the peri-hematoma immediately adjacent to the hematoma. Typically, research in this field limits biochemical assays to a comparison of the ipsilateral hemisphere to the contralateral hemisphere (or tissue from sham animals).[9,18] Although this provides valuable information, important biochemical changes within the peri-hematoma may be missed due to the dilution effect associated with tissue homogenization. Investigation of therapies to target iron toxicity would be strengthened with a better analysis of the peri-hematoma region, such as direct demonstration that increased nonheme Fe occurs colocalized with oxidative stress and cell death.

Histochemical stains for Fe also suffer from several limitations. For example, the Perls and Turnbull stains predominantly detect ferric and ferrous Fe in ferrihydrite contained within ferritin or hemosiderin and are much less sensitive to other forms of Fe. Since it takes several days for Fe released from hemoglobin breakdown to be incorporated into hemosiderin, histochemical analysis of Fe distribution is relevant only for hemorrhages that are at least several days old.[20−22] The Perls and Turnbull stains are not applicable to recent hemorrhages in which the chemical form of Fe is either hemoglobin or labile reactive Fe products released by uncontrolled hemoglobin breakdown.[20−22] Therefore, a major benefit to this research field would be a suite of imaging techniques capable of imaging and colocalizing hemoglobin, total Fe, and biochemical markers of oxidative damage, which has not previously been possible.

As an alternative to histochemical staining for ferric Fe or ferrous Fe, X-ray fluorescence imaging (XFI) has found increased use to image total Fe in the brain.[18,23−32] XFI detects all chemical forms of Fe and does not display preferential specificity for certain chemical forms or suffer from nonspecific binding. As such, XFI has been a valuable technique to study the distribution of brain Fe following events such as ICH and traumatic brain injury.[18,28] However, as XFI cannot differentiate between heme Fe and nonheme Fe, accurate identification of the hematoma boundary is difficult. It is generally assumed that the greatest Fe concentration is observed at the site of hemorrhage and the transition to lower Fe concentration marks the approximate hematoma boundary. However, this approach is subjective and does not provide the anatomical precision to accurately quantify the Fe concentration in the peri-hematoma zone. Likewise, red blood cells can also spread into parenchyma in smaller pools (e.g., along white matter tracts), which makes it hard to draw any simple demarcation lines. Therefore, an approach capable of accurately defining the hematoma boundary through direct imaging of hemoglobin, allowing the total Fe concentration to be quantified in the adjacent peri-hematoma zone (without contamination from hemoglobin signal), would be advantageous.

A spectroscopic technique well-suited to image the distribution of hemoglobin is resonance Raman spectroscopy. Resonance Raman spectroscopy can be used to selectively enhance vibrational modes of heme groups to image the distribution of hemoglobin.[33] Specifically, the resonance Raman spectrum of hemoglobin obtained with excitation at 514 nm contains bands assigned to oxy- and deoxy-hemoglobin (i.e., ν19 and ν10 modes at 1545 and 1582 cm^{-1}, respectively).[33,34] This property has been used to image the distribution of deoxy-

DOI: 10.1021/acschemneuro.5b00037
ACS Chem. Neurosci. 2015, 6, 761−770

and oxy-hemoglobin in arterial and venous tissues.[33] In addition, the resonance Raman enhancement is in excess of 1000× stronger than nonresonance Raman signal, allowing selective imaging of heme components in complex biological samples.[33] Because resonance Raman spectroscopy in nondestructive, it can be performed prior to XFI such that images of hemoglobin and total Fe can be obtained from the same tissue section.

In addition to XFI and resonance Raman spectroscopy, a third spectroscopic technique, Fourier transform infrared spectroscopic imaging (FTIRI), holds great potential to study protein aggregation.[26,35−41] Furthermore, it is established that free Fe induces the formation of high molecular weight protein aggregates.[42]

This investigation serves as an important method validation for the use of resonance Raman spectroscopy, XFI, and FTIRI to delineate the Fe and aggregated protein content within the hematoma and peri-hematoma zone following ICH. The results of this study demonstrate that total Fe, which is not in the chemical form of hemoglobin, is elevated within the peri-hematoma zone 1 day after ICH. Such early detection of elevated nonheme Fe has not previously been made.[9,18] Furthermore, the results of FTIRI demonstrate that protein aggregation is present to a significant extent within both the hematoma and peri-hematoma zone. This result highlights that total Fe may be a less important indicator of tissue damage than once thought, whereas the chemical form of Fe and its ability to redox cycle may be a more critical factor for mediating tissue damage. Alternatively, these results could support the possibility that other factors, such as inflammation, are more critical than Fe in mediating early tissue damage after ICH. The method validated by this study lays the foundation for future more detailed investigation of the exact mechanisms of acute and chronic tissue damage after ICH.

RESULTS AND DISCUSSION

Proof of Principle: Analysis of Fresh and Aged Blood with Resonance Raman Spectroscopy and XFI. Two drops of dried blood were prepared from fresh and aged aliquots of the same blood sample and imaged with resonance Raman spectroscopy and XFI to demonstrate the ability of two complementary techniques to differentiate between heme Fe and nonheme Fe. The visual appearance of both dried blood samples was comparable, and both dried drops displayed intense red coloration around the periphery (Figure 1A,B). The point of focus with visible light was different between the center and periphery for both dried drops, indicating a difference in thickness. The periphery of both dried drops was observed to be thicker than the center. However, the center of both dried drops shared the same focus point (i.e., equivalent thickness). Hemoglobin resonance Raman signal was observed for both drops of blood; however, the signal was substantially stronger within the center of the fresh blood relative to that at the center of the aged blood (Figure 1E−G). Within both samples, the strongest resonance Raman signal was observed to colocalize with the most intense red coloration in the visible light image, at the periphery of the dried drop. XFI revealed that the Fe concentration was greatest at the periphery of both dried drops, and the concentration of Fe within the center of the dried drops was approximately equal between the two drops (i.e., light blue pixels in the center in Figure 1C,D).

The results from the proof-of-principle experiment of fresh and aged blood demonstrate the complementary spectroscopic

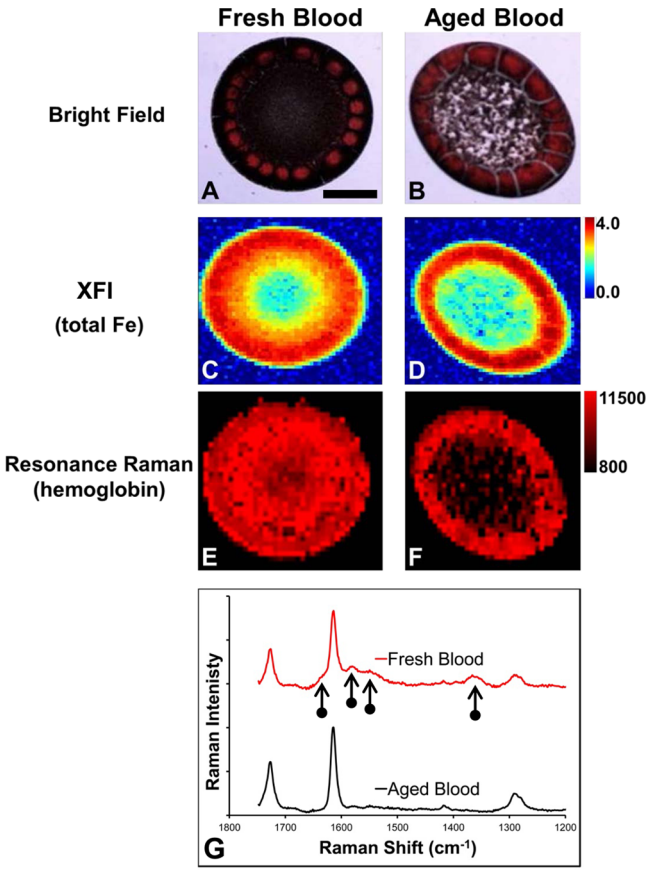

Figure 1. Resonance Raman and XFI analysis of fresh and aged blood from the proof-of-principle experiment. (A, B) Bright-field visible light images of dried drops of blood prepared from (A) fresh blood and (B) dried blood. (C, D) XFI images of total Fe in dried drops of blood prepared from (C) fresh blood and (D) aged blood. (E, F) Resonance Raman images of hemoglobin distribution in dried drops of blood prepared from (E) fresh blood and (F) aged blood. (G) Representative resonance Raman spectra (514 nm excitation) collected from fresh and aged blood. The intensity scale for panels C and D is in μg cm^{-2}. The intensity scale for panels E and F is integrated Raman counts (AU). Vertical arrows indicate characteristic resonance Raman heme bands. Scale bar = 500 μm.

approach of resonance Raman spectroscopy and XFI to study heme-Fe and total Fe. XFI detects all chemical forms of Fe and revealed that both drops of blood contained approximately equal amounts of Fe. Indeed, this would be expected for two aliquots from the same blood sample. However, XFI does not reveal any information regarding the chemical form of Fe. In contrast, resonance Raman detects heme-bound Fe. As the second blood aliquot was subjected to three freeze−thaw cycles that cause red blood cell lysis, enzymatic degradation of hemoglobin would be expected to occur during the 12 h incubations under ambient laboratory conditions. Therefore, although the total Fe content of the sample would be expected to remain the same, the majority of Fe would be expected to be released from hemoglobin and exist as free Fe or secondary reaction products in the aged blood sample. The results of resonance Raman support this, with a strong resonance Raman hemoglobin signal observed from the center of the dried drop of fresh blood but only weak signal observed from the center of the dried drop of aged blood. It is important to note that comparison between samples was made only for regions that shared the same focus point (the center of the two dried drops

DOI: 10.1021/acschemneuro.5b00037
ACS Chem. Neurosci. 2015, 6, 761−770

shared the same focus point). This is a common and well-validated approach, with numerous investigations using Raman spectroscopy to study the biochemical composition of dried drops of biological fluids.[43,44] Because the edge of the dried drops was thicker, it did not share the same focus point, and reliable comparisons cannot be made for this region.

Characterization of the Hematoma Boundary and Quantification of Nonheme Fe in the Peri-hematoma Zone 24 h after Hemorrhagic Stroke Using Resonance Raman Spectroscopy and XFI. *Histology.* To characterize the hematoma boundary, visible light microscopy images were taken from unstained tissue and tissue sections stained with hematoxylin and eosin (H&E) or cresyl violet (Figure 2). The

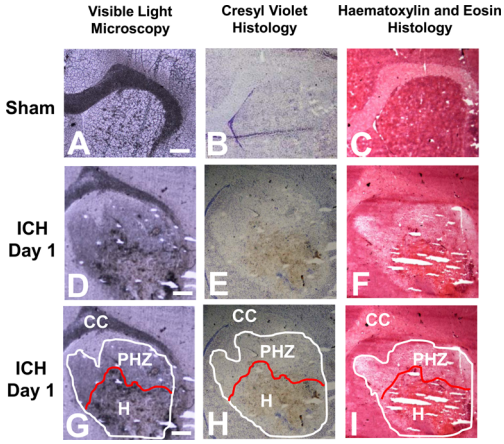

Figure 2. Visible light microscopy and histological characterization of the hematoma boundary following ICH. Visible light microscopy of (A, D, G) unstained tissue sections, (B, E, H) cresyl violet stained tissue sections, and (C, F, I) H&E stained tissue sections. (A–C) Sham tissue. (D–F) Tissue 1 day after ICH. (G–I) Tissue 1 day after ICH with annotations to demarcate hematoma boundary (H) and peri-hematoma boundary (PHZ) (based on spread of edema into the tissue). Scale bar = 500 μm.

hematoma boundary was defined by blood by dark red/black coloration in the unstained tissue from animals 1 day after ICH (Figure 2D), brown coloration in the cresyl violet stained tissue (Figure 2E), and bright orange coloration in the H&E stained tissue (Figure 2F). It is important to note that the coloration of blood in Figure 2D,E is not a result of any staining but rather is the natural pigment of blood, as described by others.[21] The tissue surrounding the hematoma showed distinct characteristics of edema, such as a darker coloration compared to unstained tissue (Figure 2D) and lighter staining with both cresyl violet and H&E (Figure 2E,F). These histological markers allowed identification of the hematoma and the spread of edema into the peri-hematoma zone, which has been annotated in Figure 2G–I. The annotation presented in Figure 2G–I was used as a guide to calculate the average Fe and aggregated protein concentration within the hematoma and peri-hematoma zone from XFI and FTIRI analyses.

As Perls and Turnbull stain predominantly detects Fe bound within hemosiderin, positive staining within 24 h of ICH is either minimial[9] or not observed,[21] in contrast to staining at later time points following hemoglobin breakdown and storage of excess Fe within the hemosiderin complex.[9] This is demonstrated in this study in Supporting Information Figure 1, in which tissue sections from a representative animal 1 day after ICH showed negative Perls staining, whereas strong Perls staining was observed in tissue from animals 7 and 14 days after ICH.

Resonance Raman Spectroscopic Mapping of the Hematoma Boundary. In order to accurately identify the hematoma/peri-hematoma boundary, resonance Raman spectroscopy was used to study the distribution of hemoglobin. Hemoglobin distribution was visualized in tissue sections using the integrated area from 1535–1590 cm^{-1} (ν19 bands of oxy- and deoxy-hemoglobin),[33,34] detected by resonance Raman spectroscopic mapping with 514 nm excitation. To allow visualization of the hemoglobin signal from the hemorrhage that is above the background signal endogenous to brain tissue, the scaling of resonance Raman images was set so the minimum pixel value that was equal to the maximum intensity observed for all sham animals. For example, the maximum integrated band area (arbitrary units, AU) for sham animals was 300 (AU), so the minimum pixel intensity was set to 300 (AU) for all images. Therefore, in the resonance Raman images, all pixels that display coloration represent signal greater than that observed in sham animals. Using this approach, the intense hemoglobin signal provides objective and reproducible identification of the hematoma boundary. The visible light microscopy images of unstained tissue sections of sham animals and animal 1 day after ICH are presented in Figure 3A,E. Representative resonance Raman spectroscopic maps of the distribution of hemoglobin in sham animals and animals 1 day after ICH are presented in Figure 3B,F. Representative spectra taken from individual pixels that correspond to the hematoma, hematoma/peri-hematoma boundary, and the peri-hematoma are presented in Figure 4 and clearly highlight the strong resonance Raman signal from hemoglobin observed within the hematoma boundary, which is absent immediately adjacent to the boundary. For all samples, no resonance Raman signal was observed at distances farther from the hematoma/peri-hematoma boundary, unless there was an obvious blood vessel (Figures 3B,F and 4 are representative examples). Tissue regions that contained an obvious blood vessel were excluded from analysis. Using the resonance Raman images of hemoglobin to define the hematoma/peri-hematoma boundary, a region of interest was determined for the peri-hematoma zone that extends for 500 μm from the hematoma/peri-hematoma boundary (annotated in Figure 3E–H). A similar-sized region of interest was drawn within the hematoma and also for sham tissue. The above regions of interest were used to calculate the average Fe and aggregated protein content from XFI and FTIRI experiments, respectively.

XFI Elemental Mapping of Fe Distribution within the Hematoma and Peri-hematoma Zone. Total Fe distribution was imaged using XFI elemental mapping with a synchrotron light source. Representative Fe elemental maps from a sham animal and an animal 1 day after ICH are presented in Figure 3C,G. As expected, there is an obvious visual increase in Fe concentration in the brain tissue 1 day after ICH relative to that in the sham animal. The greatest Fe concentration is observed within the hematoma zone (labeled H in Figure 3E), and subtly increased Fe appears to border the region of greatest Fe concentration. Overlay of XFI maps of total Fe with resonance Raman maps of hemoglobin confirmed that this location is the peri-hematoma zone (labeled PHZ in Figure 3F). We note that the XFI image alone does not specifically locate the hematoma/peri-hematoma boundary and that the resonance Raman images are required for definitive identification of the hematoma/peri-hematoma boundary.

DOI: 10.1021/acschemneuro.5b00037
ACS Chem. Neurosci. 2015, 6, 761–770

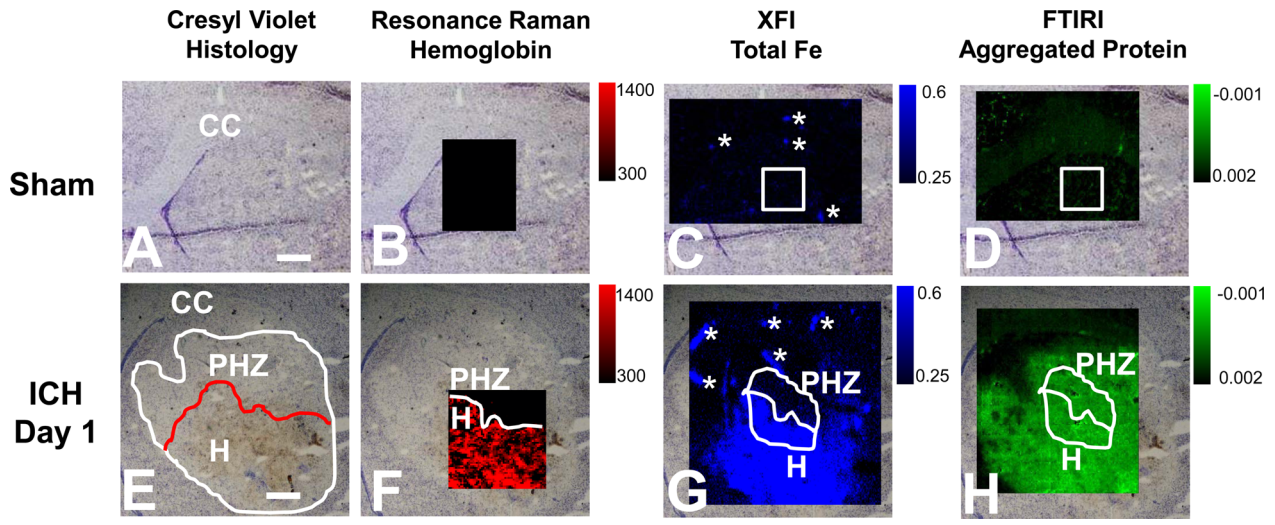

Figure 3. Resonance Raman, XFI and FTIRI analysis of the distribution of hemoglobin, total Fe, and aggregated protein in the rat striatum 1 day after ICH. (A–D) Representative images from a sham animal. (E–H) Representative images from an animal 1 day after ICH. (A, E) Visible light microscopy images of the unstained tissue. (B, F) Resonance Raman images of hemoglobin distribution. (C, G) XFI images of total Fe distribution. (D, H) FTIRI images of the aggregated protein distribution. Regions of interest that correspond to the hematoma (H) and peri-hematoma zone (PHZ) and a similar-sized area in sham animals have been annotated in white. The intensity scale for panels B and F is integrated Raman counts (AU). The intensity scale for panels C and G is in μg cm^{-2}. The intensity scale bar for panels D and H is second-derivative intensity (AU). Scale bar = 500 μm. Asterisks indicate the location of blood vessels, which were excluded from analysis.

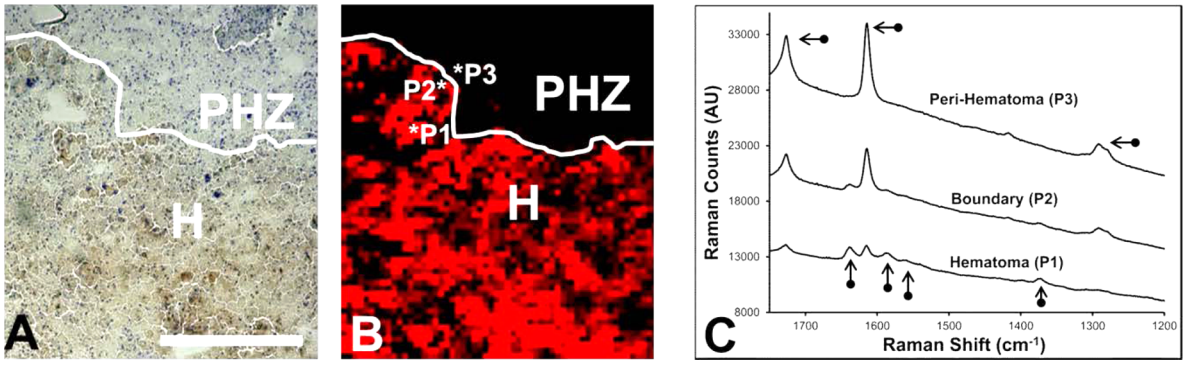

Figure 4. Representative resonance Raman spectra. (A) Cresyl violet histology showing the hematoma (H) and peri-hematoma zone (PHZ). (B) Enlarged resonance Raman map from Figure 3F. (C) Resonance Raman spectra extracted from positions that correspond to the hematoma (P1), hematoma/peri-hematoma boundary (P2), and peri-hematoma (P3). Vertical arrows indicate characteristic resonance Raman heme bands. Horizontal arrows indicate bands from the plastic thermanox substrate. Scale bar = 500 μm.

The total Fe concentration was calculated for regions of the hematoma and peri-hematoma zone (hematoma boundary to 500 μm away from the boundary). The location of the hematoma and peri-hematoma zone is annotated in Figure 3E–H, and the average Fe concentrations for the tissue zones are presented in Figure 5. The average Fe concentration was 0.90 μg cm^{-2} within the hematoma, 0.32 μg cm^{-2} within the peri-hematoma, and 0.22 μg cm^{-2} in sham animals. Fe concentration was significantly increased within the hematoma ($p < 0.001$) and peri-hematoma ($p < 0.001$) relative to that in sham animals. The Fe concentration was significantly increased within the hematoma relative to that in the peri-hematoma zone ($p < 0.001$). As no resonance Raman signal was present within the peri-hematoma zone, the increase in Fe concentration is not in the chemical form of hemoglobin.

The exact source of the elevated Fe within the peri-hematoma zone was not determined in this study. Likely possibilities include free Fe released from hemoglobin breakdown, Fe contained within plasma proteins, such as transferrin, which have diffused beyond the hematoma boundary, or Fe contained within macrophages and microglia that have migrated to the site of tissue injury.[9,10,45]

FTIRI Reveals a Significant Increase in Aggregated Protein within the Hematoma and Peri-hematoma Zone. The results from FTIRI revealed that aggregated proteins are elevated within the hematoma and peri-hematoma zone relative to that in the sham group (Figure 3D,H). Curve fitting of the average spectra for the regions of interest that correspond to the hematoma and peri-hematoma zone, as well as the average spectrum for sham animals, revealed a significant increase in the integrated band area attributed to aggregated protein in the peri-hematoma zone (0.10 AU, $p = 0.005$) and the hematoma zone (0.10 AU, $p = 0.013$) relative to that in sham animals (0.056 AU) (Figure 6). However, no significant difference was observed between the hematoma and peri-hematoma zone ($p = 0.992$). A representative example of the curve fitting procedure used is presented in Supporting Information Figure 2. Similar results were observed from analysis of second-derivative intensities, with a significant increase in second-derivative intensity observed at 1625 cm^{-1} within the peri-hematoma

DOI: 10.1021/acschemneuro.5b00037
ACS Chem. Neurosci. 2015, 6, 761–770

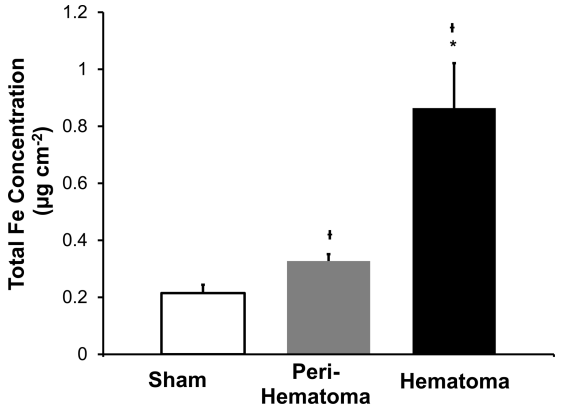

Figure 5. Quantification of total Fe from sham animals and the hematoma and peri-hematoma zone from ICH rats 1 day after ICH. Data are shown as the mean ± SD. Dagger (†) indicates a significant difference relative to sham animals. Asterisk (*) indicates a significant difference between the hematoma and peri-hematoma zone. Each group contained six animals. A significant difference was determined using a one-way ANOVA and two-tailed posthoc test (as described in Methods) and 95% confidence limit (p = 0.05).

zone (0.000092 AU, $p < 0.001$) and the hematoma (0.000085 AU, $p = 0.002$) relative to that in sham animals (0.00025 AU). No significant difference in second-derivative intensity was observed between the hematoma and peri-hematoma zone (p = 0.99). Representative spectra of the peri-hematoma, hematoma, and sham tissue are presented in Figure 6, which shows the characteristic second-derivative peak at ∼1625 cm^{-1}, diagnostic of high molecular weight protein aggregates.[46−48] It is well-established that oxidative damage to proteins results in the formation of high molecular weight protein aggregates.[42,49,50] Indeed, Fe-mediated oxidative damage is a major cause of protein aggregation, as demonstrated *in vitro*.[42] Therefore, the most likely cause of the increase in protein aggregates observed in this study is oxidative damage. However, it must be stated that other biological processes that cause protein misfolding could also contribute. Similarly, although Fe is known to mediate oxidative stress and protein aggregation *in vitro*, the data from this study does not explicitly delineate that Fe-mediated oxidative stress is the cause of protein aggregation.

The combined results of resonance Raman, XFI, and FTIRI suggest that increased total Fe within the hematoma relative to the peri-hematoma zone does not necessarily result in increased oxidative stress and tissue damage following ICH. For example, although there is significantly more Fe present within the hematoma relative to that in the peri-hematoma zone, no significant difference was observed in the aggregated protein content. Therefore, although a large amount of Fe is released into the brain parenchyma at the time of ICH, this likely does not directly participate in mediating tissue damage while it is in the chemical form of hemoglobin contained within red blood cells. Rather, it may take several days or weeks for the Fe contained within the red blood cells to be released into the surrounding tissue. The observation of a subtle increase in

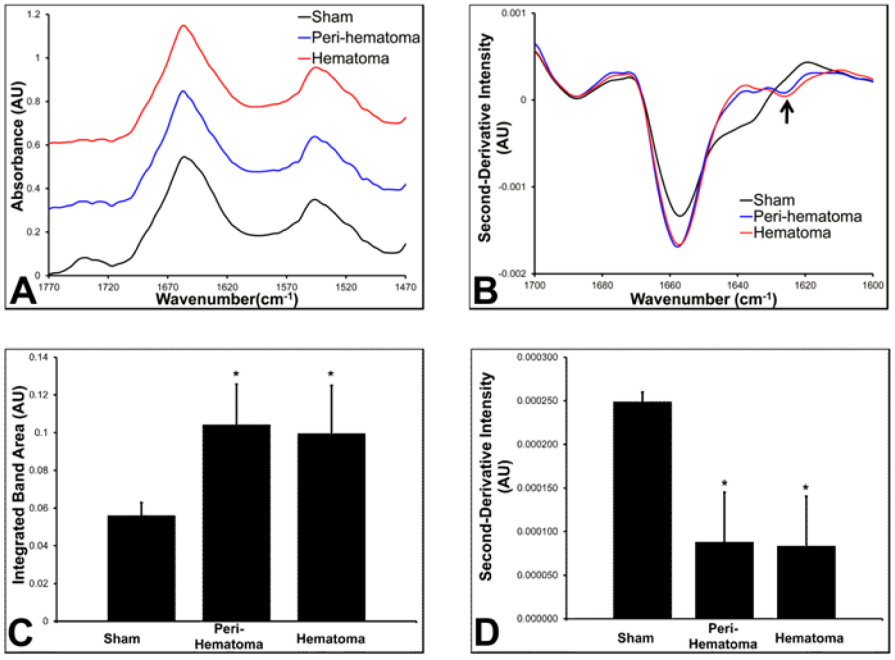

Figure 6. FTIRI analysis of the relative aggregated protein content. (A) Normalized nonderivatized FTIR spectra from a representative sham animal and the hematoma and peri-hematoma zone in an animal 1 day after ICH. Spectra have been offset vertically for clarity. (B) Second-derivative FTIR spectra from a representative sham animal and the hematoma and peri-hematoma zone in an animal 1 day after ICH. The difference in spectra intensity at 1625 cm^{-1} between the blue and red spectra is not significant. Arrow indicates location (1625 cm^{-1}) of the characteristic second-derivative minima of aggregated proteins. (C) Average integrated band area for the band centered at 1625 cm^{-1} (aggregated protein) from the results of curve fitting spectra from sham animals and the hematoma and peri-hematoma zone 1 day after ICH. (D) Average second-derivative intensity at 1625 cm^{-1} from sham animals and the hematoma and peri-hematoma zone 1 day after ICH. Dagger (†) indicates a significant difference relative to sham animals. Asterisk (*) indicates a significant difference between the hematoma and peri-hematoma zone. Each group contained six animals. Data in panels C and D are shown as the mean ± SD. A significant difference was determined using a one-way ANOVA and two-tailed posthoc test (as described in Methods) and 95% confidence limit (p = 0.05). Note that in second-derivative spectra increased concentration results in lower (more negative intensity) values.

DOI: 10.1021/acschemneuro.5b00037
ACS Chem. Neurosci. 2015, 6, 761−770

nonheme Fe within the peri-hematoma zone, alongside an increase in aggregated protein content, may fit with the hypothesis of free-Fe-mediated oxidative stress following release of Fe from hemoglobin. If so, then the results of this study suggest that the chemical form of Fe is a more important factor in mediating tissue damage, not the absolute concentration of Fe present. However, the subtle increase in Fe concentration could also be the result of infiltrating macrophages and microglia and might not be a source of free radical generation.[8,9,11] Under these circumstances, the results would indicate that other mechanisms are involved in tissue damage during the acute phase after ICH, (i.e., within 24 h), such as edema, inflammation, or, in some cases, ischemia. Further studies employing high spatial resolution imaging to localize these chemical changes at the subcellular level, in addition to immuno-histochemical analysis of the distribution of macrophages and microglia following ICH, will be required to reveal further information on the role of Fe-mediated toxicity following ICH.

CONCLUSIONS

This studied has employed a multimodal approach of resonance Raman spectroscopy, XFI, and FTIRI to study the distribution of hemoglobin, total Fe, and aggregated protein 1 day after collagenase-induced ICH in rats. The results provided accurate demarcation of the hematoma/peri-hematoma boundary, revealing a large increase in total Fe within the hematoma, which is primarily hemoglobin, and a subtle but significant increase in Fe within the peri-hematoma zone, which is not in the chemical form of hemoglobin. Both the hematoma and peri-hematoma zone contained a significant increase in aggregated protein content relative to control tissue, but no significant difference was observed between the hematoma and immediate peri-hematoma zone. These results highlight that the chemical form of Fe, rather than the total Fe concentration, may be a more important mediator of oxidative stress and tissue damage. In addition, the results of this study showed a discrepancy in the distribution of Fe and aggregated protein content within the peri-hematoma zone. Although a large decrease in the total Fe concentration was observed at the hematoma/peri-hematoma boundary, the aggregated protein content remained constant. Therefore, free radicals may propagate through the tissue away from their originating Fe source, or, more likely, other mechanisms may be involved in mediating tissue damage within the acute period after ICH. Future studies will use the analytical approach developed and validated in this study to monitor the spread of Fe, the kinetics of hemoglobin breakdown, and protein aggregate formation across an extended time course following ICH. Such time course studies are needed to design and optimize therapies following ICH in humans.

METHODS

Preparation of Dried Blood Samples for Proof-of-Principle Experiment. As a proof-of-principle experiment, resonance Raman analysis and XFI analysis were performed on dried drops of blood prepared from two samples. Arterial blood was obtained from a naïve rat. For the first blood sample (blood sample 1), a 1 μL drop was placed on a metal-free plastic thermanox coverslip (Thermo Scientific) and allowed to air dry. Resonance Raman spectroscopic analysis was performed immediately. The second blood sample (blood sample 2) was subjected to three freeze−thaw cycles (to lyse erythrocytes) and allowed to stand under ambient laboratory conditions for 12 h between each cycle. A dried drop of blood was then prepared as for blood sample 1, and resonance Raman spectroscopic analysis was performed immediately. The focal plane was set to the center of both dried drops, and it was found that both dried drops shared the same focal plane. This method of drop drying biological samples for Raman analysis has been previously reported.[43,44] Following resonance Raman analysis, the dried drops of blood were kept in a desiccator in a dust-free environment until XFI analysis, which was performed 1 week later.

Collagenase Intracerebral Hemorrhage (ICH) Surgery. Surgical procedures were performed aseptically as previously described.[18] Briefly, young adult male Sprague−Dawley rats (Biosciences breeding colony at the University of Alberta) were anaesthetized with isoflurane (4% induction, 2−2.5% maintenance, 60% N_2O balance O_2), and a hole was drilled 3.5 mm right and 0.5 mm anterior to Bregma into the skull. A 26-gauge Hamilton needle (Hamilton, Reno, NV) was inserted 6.5 mm deep from the surface of the skull, and 0.14 U of collagenase (ICH group, Type IV−S collagenase, Sigma) in 1 μL of saline was infused into the striatum. Collagenase breaks down the basal lamina of blood vessels, resulting in bleeding from multiple vessels over the course of several hours.[7,51] This is a widely used model of ICH in rodents. Only saline was infused in the sham group. The wound was closed, and Marcaine was applied to diminish postoperative pain. During surgery, rectal temperature was maintained at 37 °C ± 0.5. A total of 12 animals were used in this study, which corresponded to six sham animals and six animals 1 day after ICH. These procedures were approved by the Biosciences Animal Care and Use Committee at the University of Alberta and were in accordance with the guidelines of the Canadian Council for Animal Care.

Tissue Preparation and Tissue Sectioning. Brain tissue was prepared as previously described.[52] In general, rats were anaesthetised with isoflurane and killed via decapitation. The head immediately went into liquid nitrogen to freeze the sample within <30 s. The frozen rat brain was chiseled out from the frozen rat head on dry ice. Coronal tissue sections were cut at a Bregma location between 1 and 2 mm anterior to Bregma, which corresponded to the center of the hematoma within the striatum. The tissue sections were cut using a cryo-microtome at −18 °C, at a thickness of 20 μm. For each animal, four serial sections were cut: one section was mounted on metal-free thermanox plastic coverslips for resonance Raman and XFI analysis, one section was mounted on CaF_2 for FTIRI analysis, and two sections were mounted on regular glass microscope slides for H&E and Perls histology. In addition, following resonance Raman and XFI analysis, the tissue section mounted on the thermanox plastic coverslip was also stained with cresyl violet. The tissue sections were air-dried prior to Raman spectroscopic analysis. All Raman spectroscopic analysis was performed within 24 h of tissue sectioning. Following Raman spectroscopic analysis, tissue sections were stored in the dark on desiccant until XFI analyses (1 week later). The Raman spectrum of the blank coverslip was recorded to confirm that bands from the plastic polymer would not interfere with the Raman mapping.

Resonance Raman Spectroscopic Mapping. Resonance Raman spectroscopic mapping of the distribution of hemoglobin was performed with a Reflex spectrometer controlled with Renishaw WiRE software (Renishaw, WiRE, version 3.3). The inVia Reflex spectrometer is equipped with an air-cooled charge-coupled device (CCD) camera and a Leica DMLM microscope. Sample excitation and selective resonance enhancement of heme moieties of hemoglobin was achieved using an Ar+ laser (Modu-Laser, UT, USA) emitting at 514.5 nm. Stokes Raman spectra were collected using a 1200 mm/line grating across the spectral range of 1900−650 cm^{-1}. Spectra were collected with a 50× microscope objective, using 100% laser power, with an accumulation time of 10 s and an effective step size of 20 μm in streamline mapping mode. The size of the maps collected ranged from 100 × 100 μm^2 to 500 × 500 μm^2. Data analysis and maps of hemoglobin distribution were generated with Renishaw WiRE software (Renishaw, WiRE, version 3.3). Well-established resonance Raman marker bands of hemoglobin were used to generate maps, with the integrated area calculated from 1535−1590 cm^{-1}, to include both the bands centered at 1545 and 1582 cm^{-1} (ν19 mode) (combined oxy- and deoxy-hemoglobin).[33,34] No attempt was made to differ-

DOI: 10.1021/acschemneuro.5b00037
ACS Chem. Neurosci. 2015, 6, 761−770

entiate between oxy- and deoxy- hemoglobin in this initial investigation, but future time course studies will use resonance Raman spectroscopy to evaluate the oxygenation state of hemoglobin following ICH. Note that due to the longer image collection time associated with resonance Raman spectroscopy relative to XFI and FTIRI a smaller area of analysis was performed with resonance Raman spectroscopy.

Synchrotron Radiation XFI. Elemental maps were collected with XFI using synchrotron light at beamline 10-2 at the Stanford Synchrotron Radiation Lightsource (SSRL) (http://www-ssrl.slac.stanford.edu/beamlines/bl10-2/). The energy of the incident X-ray beam was 13 450 eV, and the incident X-ray intensity was measured using a nitrogen gas-filled ion chamber. A monocapillary optic (XOS, East Greenbush, NY, USA) was positioned with its output 1 mm away from the samples, resulting in a X-ray spot size of approximately 25 μm at the sample. The sample was mounted at 45° to the incident beam and rastered through the beam, with a beam exposure time of 200 ms per 20 μm step. A 4-element Vortex silicon drift detector at 90° to the incident beam collected the X-ray fluorescence spectra from the brain tissue. The detector readout was synchronized to the stage movement speed, and data were collected continuously such that the full emission spectrum was collected every 200 ms, for an average stage movement of 20 μm. This method of rapid scanning has been described previously.[31] The full emission spectrum was recorded at each pixel (multichannel analysis, MCA), in addition to single channels for P, S, Cl, K, Ca, Fe, Cu, and Zn fluorescence lines and inelastic scatter. Since this study has sought to validate the method of multimodal XFI, resonance Raman, and FTIRI, only the results of Fe distribution are reported. Future time course studies will use all elemental information. In addition to measurements of brain sections, emission spectra were collected from an Fe calibration standard to provide quantification of Fe concentration. The Fe standard was commercially sourced from Micromatter (Vancouver) and consisted of a known concentration of Fe (56.0 μg cm^{-2}), sputter coated onto a 6 μm thick layer of mylar film. Single channel analysis of standards was used to quantify single channel data from brain tissue samples, as previously reported.[53,54] Samples were treated as thin sections, in accordance with previous studies.[55] XFI images of Fe distribution were generated using MicroTool Kit software (http://smak.sams-xrays.com/). Quantification was performed on regions of the hematoma and peri-hematoma zone (and equivalent area in sham animals) that corresponded to approximately 200 pixels (i.e., an area of 80 000 μm^2). The minimum detection limits for each element were calculated using the fluorescence signal for each standard and a blank, as described in Supporting Information,[56] and are presented in Supporting Information Table 1.

FTIRI Analysis of Relative Aggregated Protein Content. Globar-FTIR-focal plane array (FPA) spectroscopic images were collected at the Canadian Light Source (CLS) with a Hyperion 3000 microscope fitted with an upper objective of 15× magnification and a numerical aperture of 0.6 and a lower condenser of 15× magnification and 0.4 numerical aperture. This arrangement yielded a pixel size of 2.65 μm, which was later subjected to 8 × 8 pixel binning to yield an effective image pixel size of 21.4 μm (similar to the effective pixel size of XFI experiments). The FTIRI data were collected with a spectral resolution of 4 cm^{-1} and the coaddition of 32 scans, and a background image was collected from blank substrate using 32 coadded scans. The background was collected immediately prior to each sample.

All data processing and image generation were performed using Cytospec software (Cytospec, version 1.2.04) and Opus software (version 6.5, Bruker, Ettlingen, Germany). Raw spectra were vector-normalized to the amide I band (1700−1600 cm^{-1}), and second-derivatives were calculated with a Savitsky-Golay 13-point smoothing average. False color functional group images of the relative concentration of high molecular weight β-sheet aggregates were generated from the second-derivative intensity at 1625 cm^{-1}. Statistical analysis was performed on the average second-derivative intensity at 1625 cm^{-1}. To further support the analysis of second-derivative spectra, curve fitting was applied to the vector-normalized non-derivatized spectra to determine the relative content of high molecular weight β-sheet aggregates. Curve fitting was performed with a mixed Lorentzian/Gaussian line band shape, using the second-derivate spectra as a guide for the location of bands. Curve fitting was performed with Opus software (version 6.5, Bruker, Ettlingen, Germany) over the spectral range 1700−1600 cm^{-1}, using 10 bands, centered at 1690, 1680, 1673, 1665, 1656, 1646, 1636, 1625, 1616, and 1605 cm^{-1}, with least-squares minimization, similar to methods previously described.[57]

Histological and Histochemical Staining. Visible light microscopy images were captured from the unstained tissue sections prior to spectroscopic analysis with a Nikon Eclipse 50i microscope, using NIS Elements F3.0 software. Following spectroscopic analysis, tissue sections were fixed with 4% formalin solution and stained with cresyl violet. Serial tissue sections were fixed in the same manner and stained with hematoxylin and eosin (H&E) and Perls stain. For Perls histochemistry, tissue sections were incubated with equal parts 0.1 M HCl and 0.1 M ferricyanide for 30 min at room temperature, followed by rinsing off of excess reagent in deionized water, dehydration in alcohol, and counter staining with nuclear fast red. Microscopic images of the stained tissue were captured as described for the unstained tissue. Note that tissue sections from rats 7 and 14 days post ICH from a different study were used as positive controls for the Perls stain.

Data Analysis and Statistics. The aim of this investigation was to demonstrate the complementary capabilities of a novel direct biospectroscopic imaging approach to elucidate the role of Fe-induced oxidative stress and protein aggregation after ICH. To this end, this study sought to determine if nonheme Fe and aggregated protein levels were significantly increased in hematoma and peri-hematoma tissue relative to healthy tissue from sham animals. Therefore, the null hypothesis was that the Fe concentration and aggregated protein content were not significantly increased in hematoma and peri-hematoma tissue relative to that in sham animals. All data was considered as continuous quantitative parametric data (semiquantitative for FTIR data). Normality of data sets was confirmed with the Kolmogorov−Smirnov normality test. A one-way ANOVA was performed to confirm a significant effect for the concentration of Fe; $F(2,17) = 110.70$, $p < 0.001$; relative concentration of protein aggregates determined from curve fitting $F(2,17) = 12.49$, $p < 0.001$; relative concentration of protein aggregates determined from second-derivative spectra $F(2,17) = 33.72$, $p < 0.001$. Levene's test was used to test for homogeneity of variance within groups. If the Levene's test statistic was significant, then a two-tailed Dunnet T3 posthoc test that does not assume equal variance was chosen. If the Levene's test was not significant, then a two-tailed Dunnet posthoc test that assumes homogeneous variance was applied. Levene's test was significant for analysis of XFI Fe concentration data ($p = 0.004$) and FTIRI curve fitting data ($p = 0.032$), but it was not significant for FTIR second-derivative data ($p = 0.180$). The respective posthoc tests were used to reject the null hypothesis that Fe concentration or aggregated protein content was not increased within the hematoma or peri-hematoma zone relative to tissue from sham animals. The 95% confidence limit was used ($p < 0.05$). All statistical analysis was performed on six animals for each group ($n = 12$ total). All statistical analysis was performed with SPSS v. 13. It is important to note that the statistical approach used assumes normality of data. Due to the modest sample size used in this investigation ($n = 6$), it can not definitively be shown that the assumption of normality holds true. If this assumption does not hold true, then the equivalent nonparametric statistical analysis (for example Kruskal−Wallis and Mann−Whitney U test posthoc) would provide more statistical power. Therefore, the approach used in this study represents a more conservative statistical analysis. We note that when nonparametric statistical analysis was applied to this data set the same scientific conclusions were obtained (data not shown).

■ ASSOCIATED CONTENT

Ⓢ Supporting Information

Figure S1: Perls histochemistry at days 1, 7, and 14 post ICH. Figure S2: Representative examples of the curve fitting procedure of FTIR spectra. Table S1: Entire data set used for

DOI: 10.1021/acschemneuro.5b00037
ACS Chem. Neurosci. 2015, 6, 761−770

statistical analyses. This material is available free of charge via the Internet at http://pubs.acs.org.

AUTHOR INFORMATION

Corresponding Author

*E-mail: fcolbour@ualberta.ca.

Author Contributions

M.J.H. contributed 30% of experimental research and is the primary author of the manuscript. M.D. contributed 30% of the experimental research and contributed to editing the manuscript. S.C. contributed 5% of the experimental research and contributed to editing the manuscript. B.B. contributed 5% of the experimental research and contributed to editing the manuscript. H.N. contributed 10% of the experimental research and contributed to editing the manuscript. P.G.P. contributed 10% of the experimental research and contributed to editing the manuscript. F.C. contributed 10% of the experimental research and was the primary editor of the manuscript. H.N., P.G.P., and F.C. supervised this research.

Funding

This work was supported by a Canadian Institutes of Health Research (CIHR)/Heart and Stroke Foundation Synchrotron of Canada (HSFC) team grant, CIF 99472, awarded to H.N., P.G.P., F.C., and others. During the course of this study, M.J.H. was a Saskatchewan Health Research Foundation postdoctoral fellow and is currently a Canadian Institute of Health Research (CIHR) postdoctoral fellow, a postdoctoral fellow with grant CIF 99472, and a CIHR-Training Grant in Health Research Using Synchrotron Techniques (CIHR-THRUST) postdoctoral fellow.

Notes

The authors declare no competing financial interest.

ACKNOWLEDGMENTS

F.C. is a Canada Research Chair in Intracerebral Hemorrhagic Stroke. Part of the research described in this article was performed using the Hyperion 3000 infrared microscope and the Renishaw Raman Spectrometer at the Canadian Light Source, which is supported by the Natural Sciences and Engineering Research Council of Canada, the National Research Council Canada, the Canadian Institutes of Health Research, the Province of Saskatchewan, Western Economic Diversification Canada, and the University of Saskatchewan. Portions of this research were carried out at the Stanford Synchrotron Radiation Lightsource, a Directorate of SLAC National Accelerator Laboratory and an Office of Science user facility operated for the U.S. Department of Energy Office of Science by Stanford University. The SSRL Structural Molecular Biology Program is supported by the DOE Office of Biological and Environmental Research and by the National Institutes of Health, National Center for Research Resources, Biomedical Technology Program (P41RR001209). The resonance Raman spectroscopic imaging for this research was performed at the Saskatchewan Structural Sciences Center (SSSC) at The University of Saskatchewan.

ABBREVIATIONS

ICH , intracerebral hemorrhage; XFI , X-ray fluorescence imaging; FTIRI , Fourier transform infrared spectroscopic imaging

REFERENCES

(1) Qureshi, A. I., Tuhrim, S., Broderick, J. P., Batjer, H. H., Hondo, H., and Hanley, D. F. (2001) Spontaneous intracerebral hemorrhage. *N. Engl. J. Med. 344*, 1450−1460.

(2) Kirkman, M. A., Allan, S. M., and Parry-Jones, A. R. (2011) Experimental intracerebral hemorrhage: avoiding pitfalls in translational research. *J. Cereb. Blood Flow Metab. 31*, 2135−2151.

(3) MacLellan, C. L., Paquette, R., and Colbourne, F. (2012) A critical appraisal of experimental intracerebral hemorrhage research. *J. Cereb. Blood Flow Metab. 32*, 612−627.

(4) Wang, J. (2010) Preclinical and clinical research on inflammation after intracerebral hemorrhage. *Prog. Neurobiol. 92*, 463−477.

(5) Skriver, E., and Olsen, T. (1986) Tissue damage at computed tomography following resolution of intracerebral hematomas. *Acta Radiol.: Diagn. 27*, 495−500.

(6) Skriver, E., and Olsen, T. (1985) Edema and atrophy following cerebral stroke. A prospective and consecutive study. *Acta Radiol., Suppl. 369*, 43−45.

(7) MacLellan, C. L., Silasi, G., Poon, C. C., Edmundson, C. L., Buist, R., Peeling, J., and Colbourne, F. (2008) Intracerebral hemorrhage models in rat: comparing collagenase to blood infusion. *J. Cereb. Blood Flow Metab. 28*, 516−525.

(8) Keep, R. F., Hua, Y., and Xi, G. (2012) Intracerebral haemorrhage: mechanisms of injury and therapeutic targets. *Lancet Neurol. 11*, 720−731.

(9) Wu, J., Hua, Y., Keep, R. F., Nakamura, T., Hoff, J. T., and Xi, G. (2003) Iron and iron-handling proteins in the brain after intracerebral hemorrhage. *Stroke 34*, 2964−2969.

(10) Wu, J., Hua, Y., Keep, R. F., Schallert, T., Hoff, J. T., and Xi, G. (2002) Oxidative brain injury from extravasated erythrocytes after intracerebral hemorrhage. *Brain Res. 953*, 45−52.

(11) Ke, Y., and Qian, Z. M. (2007) Brain iron metabolism: neurobiology and neurochemistry. *Prog. Neurobiol. 83*, 149−173.

(12) Nguyen, A. P., Huynh, H. D., Sjovold, S. B., and Colbourne, F. (2008) Progressive brain damage and alterations in dendritic arborization after collagenase-induced intracerebral hemorrhage in rats. *Curr. Neurovasc. Res. 5*, 171−177.

(13) Nakamura, T., Keep, R. F., Hua, Y., Schallert, T., Hoff, J. T., and Xi, G. (2004) Deferoxamine-induced attenuation of brain edema and neurological deficits in a rat model of intracerebral hemorrhage. *J. Neurosurg. 100*, 672−678.

(14) Hua, Y., Nakamura, T., Keep, R. F., Wu, J., Schallert, T., Hoff, J. T., and Xi, G. (2006) Long-term effects of experimental intracerebral hemorrhage: the role of iron. *J. Neurosurg. 104*, 305−312.

(15) Wu, H., Wu, T., Li, M., and Wang, J. (2012) Efficacy of the lipid-soluble iron chelator 2,2′-dipyridyl against hemorrhagic brain injury. *Neurobiol. Dis. 45*, 388−394.

(16) Warkentin, L. M., Auriat, A. M., Wowk, S., and Colbourne, F. (2010) Failure of deferoxamine, an iron chelator, to improve outcome after collagenase-induced intracerebral hemorrhage in rats. *Brain Res. 1309*, 95−103.

(17) Caliaperumal, J., Wowk, S., Jones, S., Ma, Y., and Colbourne, F. (2013) Bipyridine, an iron chelator, does not lessen intracerebral iron-induced damage or improve outcome after intracerebral hemorrhagic stroke in rats. *Transl. Stroke Res. 4*, 719−728.

(18) Auriat, A. M., Silasi, G., Wei, Z., Paquette, R., Paterson, P., Nichol, H., and Colbourne, F. (2012) Ferric iron chelation lowers brain iron levels after intracerebral hemorrhage in rats but does not improve outcome. *Exp. Neurol. 234*, 136−143.

(19) Wu, H., Wu, T., Xu, X., Wang, J., and Wang, J. (2010) Iron toxicity in mice with collagenase-induced intracerebral hemorrhage. *J. Cereb. Blood Flow Metab. 31*, 1243−1250.

(20) Meguro, R., Asano, Y., Odagiri, S., Li, C., Iwatsuki, H., and Shoumura, K. (2007) Nonheme-iron histochemistry for light and electron microscopy: a historical, theoretical and technical review. *Arch. Histol. Cytol. 70*, 1−19.

(21) Liu, S., Grigoryan, M. M., Vasilevko, V., Sumbria, R. K., Paganini-Hill, A., Cribbs, D. H., and Fisher, M. J. (2014) Comparative

DOI: 10.1021/acschemneuro.5b00037
ACS Chem. Neurosci. 2015, 6, 761−770

analysis of H&E and Prussian blue staining in a mouse model of cerebral microbleeds. *J. Histochem. Cytochem. 62*, 767−773.
(22) Wagner, K. R., Sharp, F. R., Ardizzone, T. D., Lu, A., and Clark, J. F. (2003) Heme and iron metabolism; role in cerebral hemorrhage. *J. Cereb. Blood Flow Metab. 23*, 629−652.
(23) McRae, R., Bagchi, P., Sumalekshmy, S., and Fahrni, C. J. (2009) In situ imaging of metals in cells and tissues. *Chem. Rev. 109*, 4780−4827.
(24) Bourassa, M. W., and Miller, L. M. (2012) Metal imaging in neurodegenerative diseases. *Metallomics 4*, 721−738.
(25) Leskovjan, A. C., Kretlow, A., Lanzirotti, A., Barrea, R., Vogt, S., and Miller, L. M. (2011) Increased brain iron coincides with early plaque formation in a mouse model of Alzheimer's disease. *NeuroImage 55*, 32−38.
(26) Leskovjan, A. C., Lanzirotti, A., and Miller, L. M. (2009) Amyloid plaques in PSAPP mice bind less metal than plaques in human Alzheimer's disease. *NeuroImage 47*, 1215−1220.
(27) Chwiej, J., Adamek, D., Szczerbowska-Boruchowska, M., Krygowska-Wajs, A., Wojcik, S., Falkenberg, G., Manka, A., and Lankosz, M. (2007) Investigations of differences in iron oxidation state inside single neurons from substantia nigra of Parkinson's disease and control patients using the micro-XANES technique. *J. Biol. Inorg. Chem. 12*, 204−211.
(28) Chwiej, J., Sarapata, A., Janeczko, K., Stegowski, Z., Appel, K., and Setkowicz, Z. (2011) X-ray fluorescence analysis of long-term changes in the levels and distributions of trace elements in the rat brain following mechanical injury. *J. Biol. Inorg. Chem. 16*, 275−283.
(29) Popescu, B. F. G., George, M. J., Bergmann, U., Garachtchenko, A. V., Kelly, M. E., McCrea, R. P. E., Launing, K., Devon, R. M., George, G. N., and Hanson, A. D. (2009) Mapping metals in Parkinson's and normal brain using rapid-scanning X-ray fluorescence. *Phys. Med. Biol. 54*, 651.
(30) Popescu, B. F. G., Robinson, C. A., Chapman, L. D., and Nichol, H. (2009) Synchrotron X-ray fluorescence reveals abnormal metal distributions in brain and spinal cord in spinocerebellar ataxia: a case report. *Cerebellum 8*, 74−79.
(31) Popescu, B. F. G., Robinson, C. A., Rajput, A., Rajput, A. H., Harder, S. L., and Nichol, H. (2009) Iron, copper and zinc distribution of the cerebellum. *Cerebellum 8*, 74−79.
(32) Ciccotosto, G. D., James, S. A., Altissimo, M., Paterson, D., Vogt, S., Lai, B., de Jonge, M. D., Howard, D. L., Bush, A. I., and Cappai, R. (2014) Quantitation and localization of intracellular redox active metals by X-ray fluorescence microscopy in cortical neurons derived from APP and APLP2 knockout tissue. *Metallomics 6*, 1894−1904.
(33) Ogawa, M., Harada, Y., Yamaoka, Y., Fujita, K., Yaku, H., and Takamatsu, T. (2009) Label-free biochemical imaging of heart tissue with high-speed spontaneous Raman microscopy. *Biochem. Biophys. Res. Commun. 382*, 370−374.
(34) Torres Filho, I. P., Terner, J., Pittman, R. N., Proffitt, E., and Ward, K. R. (2008) Measurement of hemoglobin oxygen saturation using Raman microspectroscopy and 532-nm excitation. *J. Appl. Physiol. 104*, 1809−1817.
(35) Kneipp, J., Miller, L. M., Joncic, M., Kittel, M., Lasch, P., Beekes, M., and Naumann, D. (2003) In situ identification of protein structural changes in prion-infected tissue. *Biochim. Biophys. Acta, Mol. Basis Dis. 1639*, 152−158.
(36) Kretlow, A., Wang, Q., Kneipp, J., Lasch, P., Beekes, M., Miller, L., and Naumann, D. (2006) FTIR-microspectroscopy of prion-infected nervous tissue. *Biochim. Biophys. Acta 1758*, 948−959.
(37) Miller, L. M., Bourassa, M. W., and Smith, R. J. (2013) FTIR spectroscopic imaging of protein aggregation in living cells. *Biochim. Biophys. Acta, Biomembr. 1828*, 2339−2346.
(38) Wang, Q., Kretlow, A., Beekes, M., Naumann, D., and Miller, L. (2005) In situ characterization of prion protein structure and metal accumulation in scrapie-infected cells by synchrotron infrared and X-ray imaging. *Vib. Spectrosc. 38*, 61−69.
(39) Chwiej, J., Dulinska, J., Janeczko, K., Dumas, P., Eichert, D., Dudala, J., and Setkowicz, Z. (2010) Synchrotron FTIR micro-spectroscopy study of the rat hippocampal formation after pilocarpine-evoked seizures. *J. Chem. Neuroanat. 40*, 140−147.
(40) Gough, K. M., Tzadu, L., Kastyak, M. Z., Kuzyk, A. C., and Julian, R. L. (2010) Theoretical and experimental considerations for interpretation of amide I bands in tissue. *Vib. Spectrosc. 53*, 71−76.
(41) Kastyak-Ibrahim, M. Z., Nasse, M. J., Rak, M., Hirschmugl, C., Del Bigio, M. R., Albensi, B. C., and Gough, K. M. (2012) Biochemical label-free tissue imaging with subcellular-resolution synchrotron FTIR with focal plane array detector. *NeuroImage 60*, 376−383.
(42) Mirzaei, H., and Regnier, F. (2008) Protein:protein aggregation induced by protein oxidation. *J. Chromatogr. B 873*, 8−14.
(43) Filik, J., and Stone, N. (2008) Analysis of human tear fluid by Raman spectroscopy. *Anal. Chim. Acta 616*, 177−184.
(44) Ortiz, C., Zhang, D., Xie, Y., Ribbe, A. E., and Ben-Amotz, D. (2006) Validation of the drop coating deposition Raman method for protein analysis. *Anal. Biochem. 353*, 157−166.
(45) Gong, C., Hoff, J. T., and Keep, R. F. (2000) Acute inflammatory reaction following experimental intracerebral hemorrhage in rat. *Brain Res. 871*, 57−65.
(46) Ami, D., Bonecchi, L., Cali, S., Orsini, G., Tonon, G., and Doglia, S. M. (2003) FT-IR study of heterologous protein expression in recombinant *Escherichia coli* strains. *Biochim. Biophys. Acta, Gen. Subj. 1624*, 6−10.
(47) Ami, D., Natalello, A., Gatti-Lafranconi, P., Lotti, M., and Doglia, S. M. (2005) Kinetics of inclusion body formation studied in intact cells by FT-IR spectroscopy. *FEBS Lett. 579*, 3433−3436.
(48) Ami, D., Natalello, A., Taylor, G., Tonon, G., and Maria Doglia, S. (2006) Structural analysis of protein inclusion bodies by Fourier transform infrared microspectroscopy. *Biochim. Biophys. Acta, Proteins Proteomics 1764*, 793−799.
(49) Lam, H. S., Proctor, A., Nvalala, J., Morris, M. D., and Smith, W. G. (2004) Quantitative determination of low density lipoprotein oxidation by FTIR and chemometric analysis. *Lipids 39*, 687−692.
(50) Signorini, C., Ferrali, M., Ciccoli, L., L, S., Magnani, A., and Comporti, M. (1995) Iron release, membrane protein oxidation and erythrocyte ageing. *FEBS Lett. 362*, 165−170.
(51) Rosenberg, G. A., Mun-Bryce, S., Wesley, M., and Kornfeld, M. (1990) Collagenase-induced intracerebral hemorrhage in rats. *Stroke 21*, 801−807.
(52) Hackett, M. J., Borondics, F., Brown, D., Hirschmugl, C., Smith, S. E., Paterson, P. G., Nichol, H., Pickering, I. J., and George, G. N. (2013) A sub-cellular biochemical investigation of Purkinje neurons using synchrotron radiation Fourier transform infrared spectroscopic imaging with a focal plane array detector. *ACS Chem. Neurosci. 4*, 1071−1080.
(53) Webb, S. M. (2011) The MicroAnalysis Toolkit: X-ray fluorescence image processing software. *AIP Conf. Proc. 1365*, 196−199.
(54) Alaverdashvili, M., Hackett, M. J., Pickering, I. J., and Paterson, P. G. (2014) Laminar-specific distribution of zinc: evidence for presence of layer IV in forelimb motor cortex in the rat. *NeuroImage 103*, 503−510.
(55) Szczerbowska-Boruchowska, M. (2012) Sample thickness considerations for quantitative X-ray fluorescence analysis of the soft and skeletal tissues of the human body—theoretical evaluation and experimental validation. *X-Ray Spectrom. 41*, 328−337.
(56) Taylor, J. R. (1997) *An Introduction to Error Analysis*, 2 ed., University Science Books, Sausalito, CA.
(57) Petibois, C., and Deleris, G. (2006) Chemical mapping of tumor progression by FT-IR imaging: towards molecular histopathology. *Trends Biotechnol. 24*, 455−462.

DOI: 10.1021/acschemneuro.5b00037
ACS Chem. Neurosci. 2015, 6, 761−770